Peer-reviewed version available at Metals 2018, 8, 373; doi:10.3390/met8060373

Article

Effect of micro-segregation on impact toughness of 2.25Cr-1Mo steel after post weld heat treatment

Hyesung Na[1], Sanghoon Lee[2] and Chungyun Kang[1,*]

[1] Department of Materials Science and Engineering, Pusan National University, San 30 Jangjeon-dong, Geumjeong-gu, Busan 609-735, Korea; joyclubman@hanmail.net

[2] Industrial Technology Support Division, Korea Institute of Materials Science, 797 Changwondaero, Changwon 641-831, Korea; sanghlee@kims.re.kr

* Correspondence: kangcy@pusan.ac.kr; Tel.: +82-51-510-2852Academic Editor: name

Abstract: 2.25Cr-1Mo steel with high strength at high temperatures and good hydrogen resistance is widely used for power generation boiler material in high temperature and pressure use environments. Following the test evaluation of the ASME Boiler and Pressure Vessel Code, specimens from the base metal of a boiler pipe were found to have impact toughness values of 285 and 21 ft-lb, which are drastically different values. The analysis of the fracture surface of the 21 ft-lb test specimen revealed MnS inclusions, and it was found that cracks initiated at the inclusions. Observation of the cross-section of the crack propagation front revealed that cracks propagated along the ferrite regions and precipitate voids. Inclusions were also found in the 285 ft-lb impact specimen; however, the volume fraction of the inclusions was significantly less than that of the 21 ft-lb specimen. It was also found that the ferrite and carbide content of the 285 ft-lb specimen was less than 21 ft-lb specimen. The reason that the inclusions, ferrite, and carbide content differed in the two adjacent impact test specimens was analyzed. The effects of micro-segregation, such as MnS inclusions on ferrite and carbide, were compared and analyzed.

Keywords: ferrite, carbide, bainite, continuous cooling transformation (CCT) curve, charpy impact test

1. Introduction

Because of its high temperature creep strength, good hydrogen resistance, high toughness at high temperatures, and the ability to withstand high pressure hydrogen atmospheres (12–21 MPa) and high temperature (400–450 ° C) and pressure use environments, 2.25Cr -1Mo Steel is widely used as a power plant boiler pipe material. [1-4] Because of its excellent mechanical properties, 2.25Cr-1Mo steel is widely used not only in thermal power plants but also in nuclear power plants, where high stability is required. [5] However, 2.25Cr-1Mo steel is prone to reheating cracks when post weld heat treatment (PWHT) is performed to remove residual stress after welding, or cracking due to thermal stress from the heating and cooling cycles during power plant operation. [6-8] The integrity of the material is crucial, since such cracks can cause plant shutdowns and secondary hazards. Inspection of the components of a power plant is carried out according to the US ASME Boiler and Pressure Vessel Code and Nuclear Power Plant Components Certification.[9] An important quality test used to evaluate the material integrity is the Charpy V-notch impact test of fracture toughness.[10] For the base metal of boiler tubes, the impact test should also be tested under PWHT heat treatment conditions performed after the welding process. However, in the special case, the impact toughness values measured from the three impact tests can be large variability even under the same conditions. This phenomenon occasionally occurs in impact specimens taken from the same pipe and even at

Peer-reviewed version available at Metals 2018, 8, 373; doi:10.3390/met8060373

similar locations. The impact toughness of the material is affected by many parameters, such as microstructure, fraction and distribution of phase, test temperature, grain size, impact velocity, specimen shape, and notch position (sampling position of test specimen) [11-18]. In the impact test of the base metal, it was judged that there were not many variables and only the view from the metallurgy. If the material fails to meet the impact test requirements during a quality assurance inspection, it is necessary to analyze the cause and take measures to prevent recurrence. In addition, it is possible to prevent the recurrence by analyzing the cause and analyze the cause of the variation of the impact test, and it can be utilized as the basic data of the quality defect. In this study, we analyzed the variability of the impact test results of 2.25Cr-1.0Mo steel in a power plant boiler pipe to better understand the cause of the variability.

2. Experimental Procedure

The steel specimens used in this study were SA335 GR.P22. Specimens were analyzed at the 0°, 90°, and 180° positions. Composition analysis was done by optical emission spectrometer (LAB LAVM 10, SPECTRO Analytical Instruments GmbH, Kleve, Germany) and alloy components are shown in Table 1.

Table 1. Table.1 Chemical composition of 2.25Cr-1Mo steel (wt %)

Material	Chemical Composition (at. %)												
	C	Si	Mn	Cu	Ni	Cr	Mo	V	Nb	Al	P	S	Fe
P22	0.102	0.218	0.433	0.120	0.1246	2.0948	0.930	0.011	0.0023	0.0251	0.0140	0.0048	Bal
	0.097	0.227	0.443	0.124	0.1239	2.0305	0.931	0.012	0.0009	0.0247	0.0116	0.0039	Bal
	0.100	0.229	0.434	0.116	0.1230	2.0051	0.931	0.0141	0	0.0246	0.0098	0.0047	Bal
Average	0.100	0.225	0.436	0.120	0.1238	2.0435	0.931	0.0124	0.0011	0.0248	0.0118	0.0047	Bal

The base metal was PWHT annealed at 710 °C for 11 hours, and detailed heat treatment conditions are shown in Table 2. During the impact test of the PWHT specimens, the test specimens were randomly sampled at 1 / 4" thickness of the pipe (3ea X 6set). The sizes of the pipe and impact specimens are shown in Fig.1.

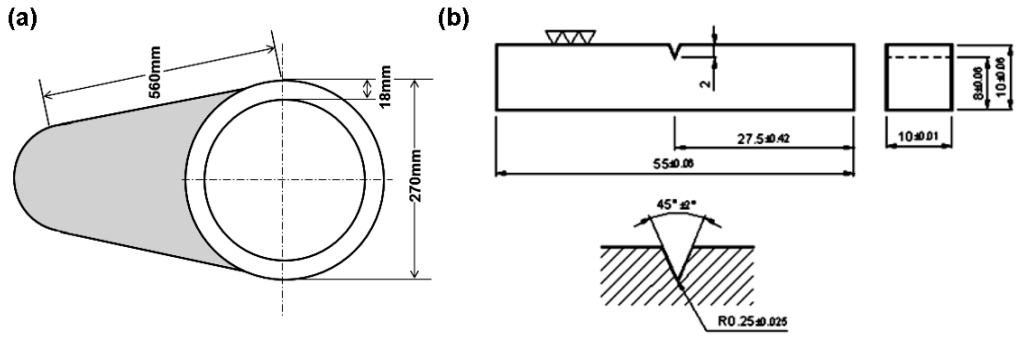

Fig.1 Schematic of pipe size and charpy V-notch impact specimen (a) pipe size (b) single-notch

The impact test was carried out at a temperature of 1 °C. Two test specimens (henceforth referred to as 285 and 21 ft-lb) with appreciable differences in impact values were selected after impact testing, and the cause of the difference of the impact values was investigated. The fracture surfaces of the specimens was observed with a stereo microscope (optical microscope, OM, Olympus BX-51M, Tokyo, Japan) and a scanning electron microscope with energy dispersive X-ray spectroscopy (SEM-EDX, SUPRA40VP, Carl Zeiss, Oberkochen, Germany), and their microstructures were analyzed with OM, SEM-EDX and electron probe microanalysis (EPMA, JXA-8530F, JEOL, Tokyo, Japan). Ferrite and carbide counting was performed using ASTM E-562 (standard test for determining volume fraction) and image analysis software (Image Pro Plus5.0, Media Cybernetics, USA). The programs

Thermo-Calc TCW5(database: TCFE6, Stockholm, Sweden, where Mats Hillert was a professor) and JMatPro 5.1 software (Sente Software, Surrey Research Park, United Kingdom) were used for state diagram and continuous cooling transformation (CCT) curve analysis.

Table 2. PWHT (Post Weld Heat Treatment) conditions of Cr-Mo steel

Condition	Actual
Loading Temperature	20℃
Heating Rate	20℃/ Hr
Holding Temperature	700 – 710℃
Holding Time	11Hr
Cooling Rate (above 425℃)	20-30℃ / Hr

3. Results and Discussion

3.1. 1 Cause analysis of crack initiation point

The purpose of this study was to analyze the variability in the impact values during impact testing. As mentioned in the Experimental Procedure section, the test specimens were randomly picked from 6 sets of 3 sets of 1 set and subjected to the impact test. In the total 6 set test piece, a test piece in the first set with a markedly different impact value was found. Fig. 2 shows the impact values of the first set and the macro-fracture surface photographs of each test specimen. The impact test values of were 285, 280 and 21 ft-lb, respectively. Two specimens had high impact values (285 and 280 ft-lb), but one specimen had a low impact value of 21 ft-lb. Only one of the 6 total sets (18ea) had an impact test value less than 100 ft-lb (5.55%). The brittle fracture surface of the specimens with low impact test values and the test specimens with high impact values were not completely destroyed, nor did ductile fractures appear.

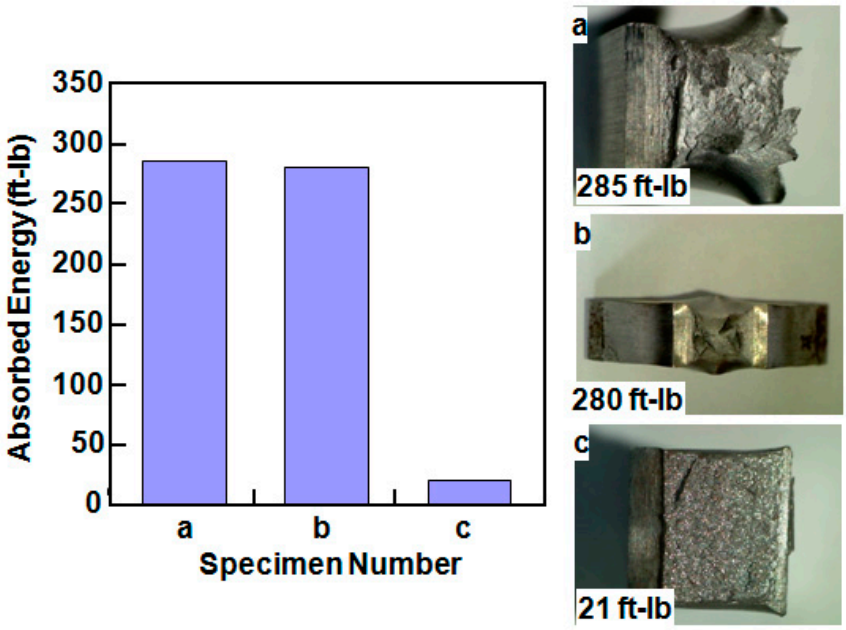

Fig.2 Absorbed energy of Charpy impact test of steel specimens (left) and corresponding images of the fractured specimens (right)

To investigate the cause of the low impact test values, the fracture surface of the 21 and 285 ft-lb test specimens were examined by SEM. The SEM images are shown in Fig.3. At position X1 in Fig. 3 (a), the 21 ft-lb test specimen showed mostly brittle fracture. When the region around X1 is enlarged, it was found that the brittle fracture originates at a particle with about a 2 μm diameter. Particles with 2 μm diameters near the point X2 were found to be MnS (Mn: 51.33% and S: 36.06%) when analyzed by SEM-EDX. It has been reported in many studies that MnS inclusions have a negative effect on mechanical properties (impact, strength, elongation) [19-21]. The low impact value of the 21 ft-lb specimen is caused by the MnS inclusion. Figure 3(b) shows SEM images of the 285 ft-lb test specimen, which has a typical ductile fracture zone where MnS inclusions were not observed. Regions where the inclusions were expected to be can be seen in various parts of the image.

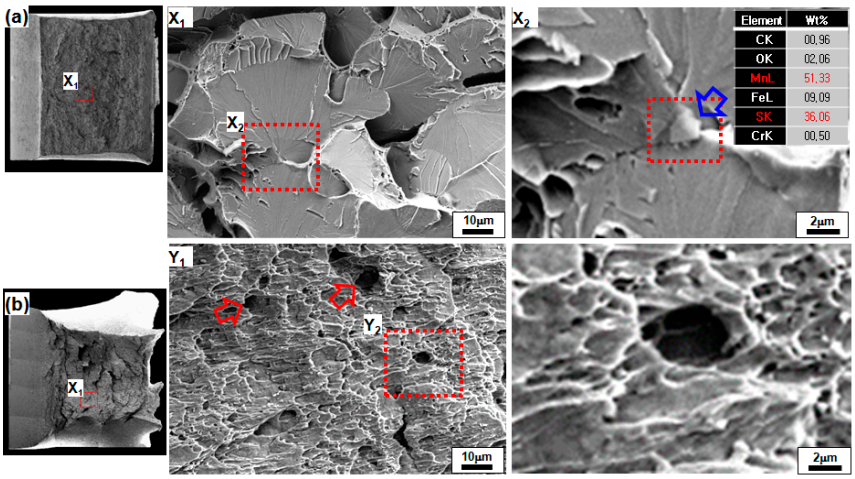

Fig.3 SEM observation of the fracture surface. (a) 21 ft-lb (b) 285ft-lb specimen

Cross-sections of the impact test specimens were examined to investigate the presence or absence of inclusions. Cross-sections of the impact test specimens were etched with Nital, then inclusions in the 21 and 285 ft-lb specimens were observed with SEM, shown in Fig. 4 (a) and (b), respectively. Observation positions were chosen to be as far from the fracture surface (red vertical lines) as possible. Inclusion shapes were examined in the region around the points X1, X2, Y1, and Y2 in Fig. 4. The inclusion sizes varied from 1 um to 10 um, and the SEM-EDX composition analysis revealed that the inclusions consisted of a complex oxide of Al oxide and MnS, and also pure Al oxide. The inclusion size and volume fraction of the 285 ft-lb impact specimen were less than those of the 21 ft-lb impact specimen.

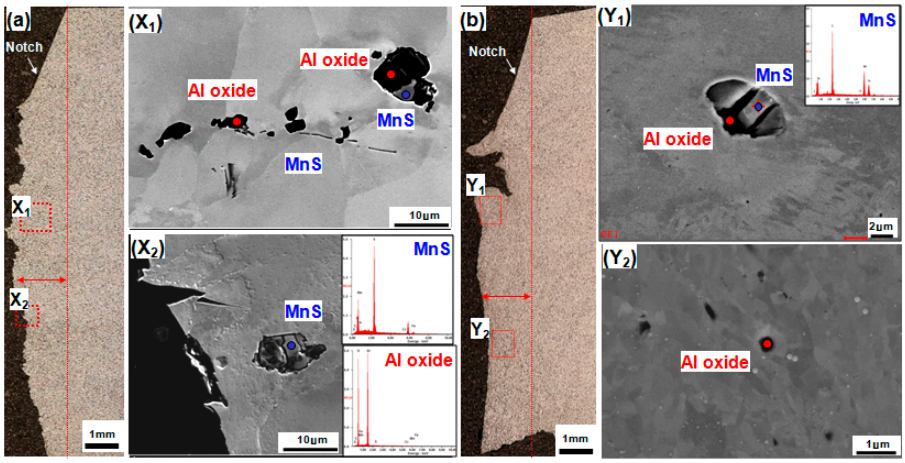

Fig.4 OM and SEM images of inclusions in the cross-section of the (a) 21 ft-lb and (b) 285 ft-lb specimen.

It has been reported in the literature that the inclusion volume fraction affects the impact value, so we measured the inclusion (MnS, AlO) volume fraction. To accurately measure the inclusion volume fraction of the two test specimens, EPMA back-scatter electron detector (BSE) images were collected and are shown in Fig. 5. In the images from EPMA-BSE, elements heavier or lighter than Fe can be observed. The elements Al, Mn, S, and O in the MnS and AlO inclusions are lighter than Fe, and appear as black regions in the EPMA-BSE images. For 2.25Cr-1Mo steel, M23C6 and M6C precipitates are observed. [22-23] One of the main elements of the precipitate is Mo, which is heavier than FE and appears as white regions in the EPMA-BSE images. [24] Fig. 5 (a) and (b) show the 21 and 285 ft-lb specimens, respectively. Black inclusions and white precipitates are observed in both specimens, however the 285 ft-lb specimen shows fewer black inclusions than the 21 ft-lb specimen. To determine the inclusion (MnS, AlO) volume fraction, we measured the total size of the black inclusion regions in 12 BSE images using image analysis software (image Pro Plus). The measured results are shown in Fig.6.

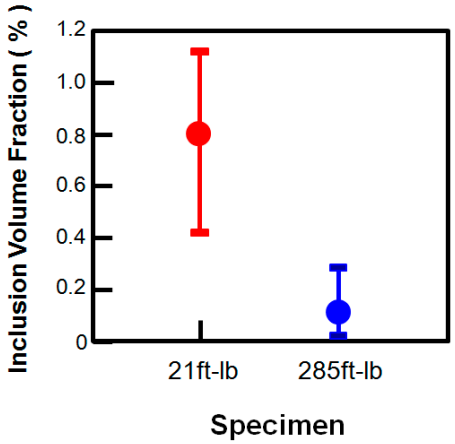

Fig.6 The experimentally measured the amount of inclusions

The inclusion volume fraction was about 0.8% for the 21ft-lb specimen and 0.1 % for the 285 ft-lb specimen. Therefore, inclusion volume fraction in the 21ft-lb specimen is about 8 times greater than the 285 ft-lb specimen. One of the reasons for the low impact value of the 21 ft-lb specimen is that the impact value decreases as the inclusion volume fraction increases, rather than simply being caused by the presence or absence of inclusions. This is consistent with a previous result reported in the literature [25]. It is evident that the inclusion volume fraction varies greatly between specimens, even within the same pipe. This has been attributed to a casting defect caused by the local incorporation of inclusions during melting and casting [26].

3.2. Cause analysis of crack propagation

As stated above, crack initiation starts at an inclusion. Cross-sections of the impact specimens were observed by SEM to identify the path of the cracks generated by the inclusions. The OM image shown in Fig. 7 (a) shows the macrostructure of the cross-section of the 21 ft-lb impact test specimen. Fig. 7 (b) shows a SEM image of the region highlighted by the red square in Fig. 7 (a). The specimen was tilted to show the fracture surface well, and then was observed by SEM. By observing from the side of the fracture surface, it is seen that the movement path of the crack can be one of two types. One type of crack propagation occurs across the ferrite, as seen in Fig. 7 (cracks across bainite were not observed, whereas crack propagation across ferrite was easily observed).

In the second type of crack propagation, a micro-void is generated in the carbide located at the grain boundary, and cracks migrate along the micro-void. Impact values are known to correlate with grain size [17]. A smaller grain size yields better impact values, and bainite with fine grain size performs well in impact tests. This is the reason that the crack propagates along the ferrite. When precipitates are present, it is known that when the coarse M23C6 carbide and M7C3 are formed at the

grain boundary,[22-23] a micro-void is formed due to the incoherent boundary between the precipitate and the matrix, and these voids combine to propagate the crack. Therefore, our results show that cracks propagate along the micro-voids around the precipitate of the grain boundaries or across the ferrite.

From the results shown in Fig. 7, the effect of the ferrite and carbide on the impact properties was estimated by comparing and analyzing the textures of the 21 ft-lb and 256 ft-lb impact test specimens.

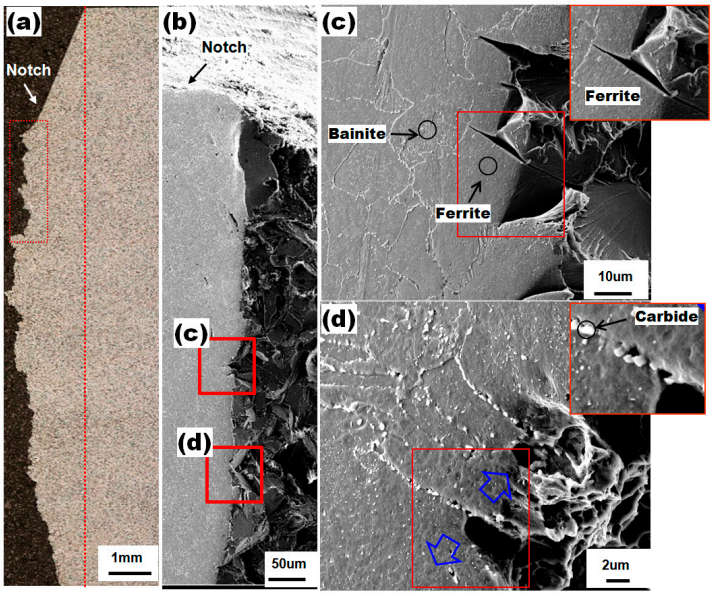

Fig.7 Microstructure of the 21 ft-lb specimen cross-section. (a) OM image, (b) SEM image, (c) and (d) SEM image of regions enclosed by the red squares in (b).

3.2.1 Effect of ferrite on impact value

Fig. 8 is a microstructure photograph of the (a) 21 ft-lb impact test specimen and (b) 256 ft-lb test specimen. Fig. 8 (c) shows the elongated ferrite + bainite structure of the 21 ft-lb specimen, and (d) shows the unstretched ferrite + bainite structure of the 265 ft-lb specimen. The ferrite fraction of (c) was higher than that of (d). The fraction of the ferrite was measured by the ASTM-E562 method by taking 16 OM images from the regions left of the red lines in Fig. 8 (a) and (b).

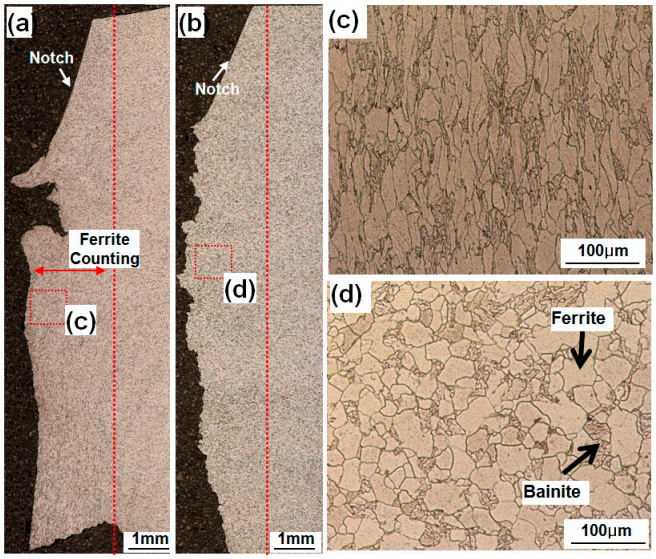

Fig.8 Microstructure of the base metal: (a) 21 ft-lb specimen and (c) is (a) part enclosed with a red square, (b) 256 ft-lb specimen and (d) is (a) part enclosed with a red square

Preprints (www.preprints.org) | NOT PEER-REVIEWED | Posted: 14 May 2018 doi:10.20944/preprints201805.0187.v1

Peer-reviewed version available at Metals 2018, 8, 373; doi:10.3390/met8060373

Fig. 9 shows the fraction of ferrite, measured from OM images. For the 256 ft-lb test specimens, the average ferrite fraction was 65.15%, while the 21 ft-lb specimen showed a high average ferrite fraction of 83.51%. Therefore, we conclude that a higher ferrite fraction yields a lower the impact value. The reason for this is that, as the fraction of ferrite increases, the fraction of bainite decreases. The impact value is lowered due to the decrease in the fraction of the bainite, which has a good impact value. The ferrite fraction of the test specimens having an impact value of 100 ft-lb was measured for 18 specimens by the same method. In Fig. 9 (b), the reliability is low due to the small number of test specimens. However, it can be seen that the correlation between ferrite fraction and impact value is linear. It is also possible to present a guideline for the fraction of ferrite required to yield the minimum required impact value, but this would require the analysis of more specimens. The two specimens shown in Fig. 9 (a) are from the same pipe. The reason for the large difference in their volume fractions is discussed below.

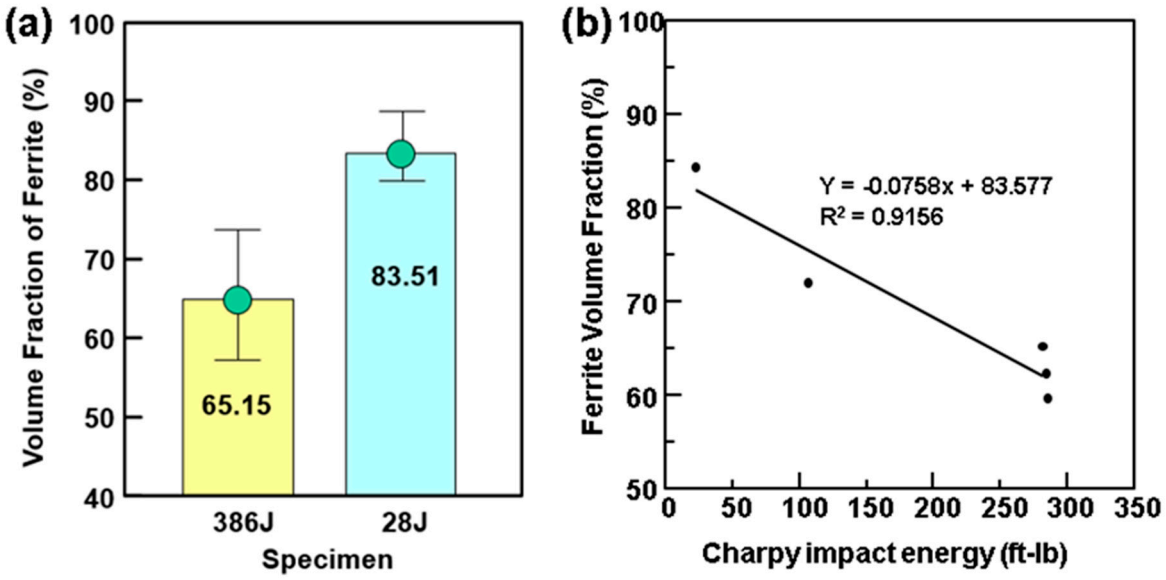

Fig.9 Relationship between volume fraction of ferrite and impact value (a) Volume fraction of ferrite for 256 and 21 ft-lb specimens, (b) liner analysis of impact value and fraction of ferrite

The 21 and 256 ft-lb test specimens contained different volume fractions of inclusions, which contained MnS. The amount of Mn in MnS is about 60%. Therefore, it is reported that a depleted zone of Mn is formed around MnS and this depleted part promotes ferrite formation.[27-28] Therefore, the volume fraction of ferrite was higher in the 21 ft-lb impact test specimen because it contained more MnS inclusions than the 256 ft-lb specimen. In more detail, the matrix composition has been described previously as a change in the Mn content of the matrix due to the difference in MnS inclusions. The composition of Mn in the matrix when the volume fraction of inclusions are 0% and about 0.05% was calculated. The calculated alloy composition is shown in Fig. 10 by a CCT curve created using Jmat-Pro. The Mn content of the matrix at 0% and 0.05% inclusions decreases from 0.436% to 0.261%.

[Total measured Mn content (0.436%) = 0.05% X Mn content in MnS (60%) + Mn content of matrix at 0.05% inclusions]

As a result, the ferrite CCT curve moves to the left as the amount of Mn decreases from 0.436% to 0.261%. At the same cooling rate (0.1 °C/sec), ferrite content increases as the ferrite moves toward shorter times along the curve. That is, as the amount of inclusions increases, the amount of Mn in the matrix decreases. As the amount of Mn in the matrix decreases, the ferrite CCT curve moves to the left, and the content of ferrite increases, even at the same cooling rate.

Preprints (www.preprints.org) | NOT PEER-REVIEWED | Posted: 14 May 2018 doi:10.20944/preprints201805.0187.v1

Peer-reviewed version available at Metals 2018, 8, 373; doi:10.3390/met8060373

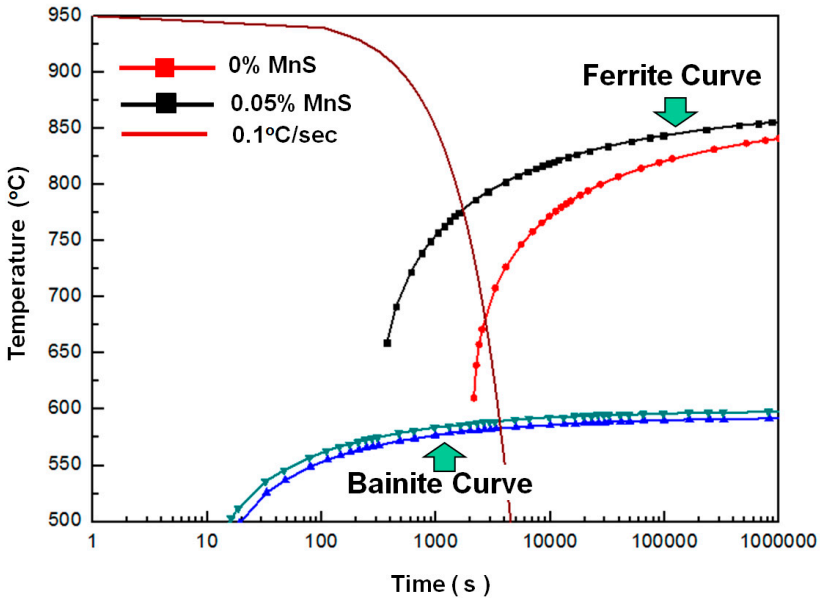

Fig.10 CCT curves for different volume fraction of alloying elements, calculated by a Jmat-Pro simulation

3.2. Effect of carbide on impact value

The microstructure in regions around the carbide in the 21 and 256 ft-lb specimens was observed. Fig. 11 shows a cross-sectional SEM image of both specimens. Inter-granular white spherical precipitates are observed, and precipitates are observed in the prior austenite grain boundary. The precipitates of Fig. 11 (d) have greater spacing and are larger in size than the prior austenite grain boundary precipitates of (c).

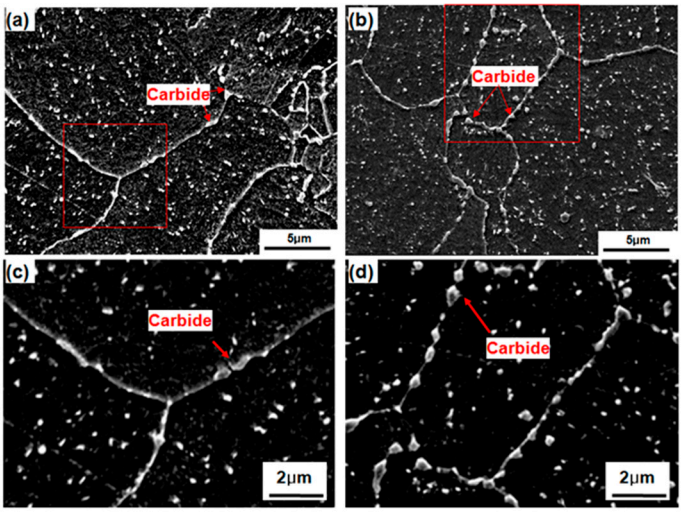

Fig.11 SEM image of the base metal (a) 256ft-lb and enlarged red square (c), (b) 21ft-lb and enlarged red square (d)

For reliable measurements, Murakami etching, a precipitate etching solution of prior austenite grain boundary, was performed. The amount and size of the precipitates were measured by using Image Pro plus. The size and size distributions of the precipitates are shown in Fig.12. The results in Fig.12 show that the size and amount of 21 ft-lb specimen precipitates are larger than the 256 ft-lb specimen. These results suggest that a large amount of large precipitates in the 21 ft-lb specimen is generated by micro-voids due to the incoherent boundary with the matrix, and then micro-voids are

Preprints (www.preprints.org) | NOT PEER-REVIEWED | Posted: 14 May 2018 doi:10.20944/preprints201805.0187.v1

Peer-reviewed version available at Metals 2018, 8, 373; doi:10.3390/met8060373

combined to propagate cracks. From the results shown in Figs. 11 and 12, the difference of the precipitates present in the two impact test specimens was investigated.

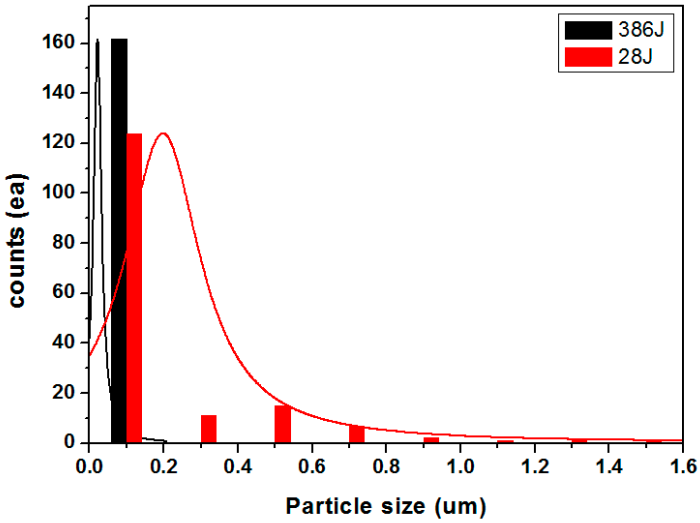

Fig.12 Histogram of a carbide in 256ft-lb and 21ft-lb specimens

Fig.13 (a) shows a well-known Fe-C phase diagram. In the Fe-C phase diagram, the C solubility in the ferrite is 0.025%. Fig.13 (b) is a state diagram of carbon content in 2.25Cr-1Mo steel using Thermo-calc. And the C solubility in the ferrite is 0.009%. The amount of C solubility varies depending on the alloying elements. Solubility of C was low in the state calculated by Thermo-Calc. This is probably due to the phase of M23C6, which takes carbon from multiple systems. In order to make a more conservative judgment, modeling was performed by calculating the amount of ferrite cabon solubility as 0.025%.

Fig.13 (c), Modeling of the carbon chemical concentration shows that the C content of ferrite is 0.025% and the C content of the base metal is 0.1%. The content of C (0.1% - 0.025% = 0.075%) must be contained in a matrix other than ferrite. The higher the ferrite content, the higher the content of C in the other matrix. Calculating the amount of carbon in the matrix of the other (non-ferrite) phase

- 21ft-lb: 0.1% C Base Metal Composition = 83.51% Ferrite Volume Fraction X 0.025% C + C content of 16.49% Matrix ==> C content of 16.49% Matrix = 0.4798%

- 56ft-lb: 0.1% C Base Metal Composition = 64.76% Ferrite Volume Fraction X 0.025% C + C content of 35.24% Matrix ==> C content of 16.49% Matrix = 0.2378%

For this reason, the amount of precipitate generated is due to the fact that the carbon content of the matrix in PWHT is twice as much as that of the matrix of 256 ft-lb.

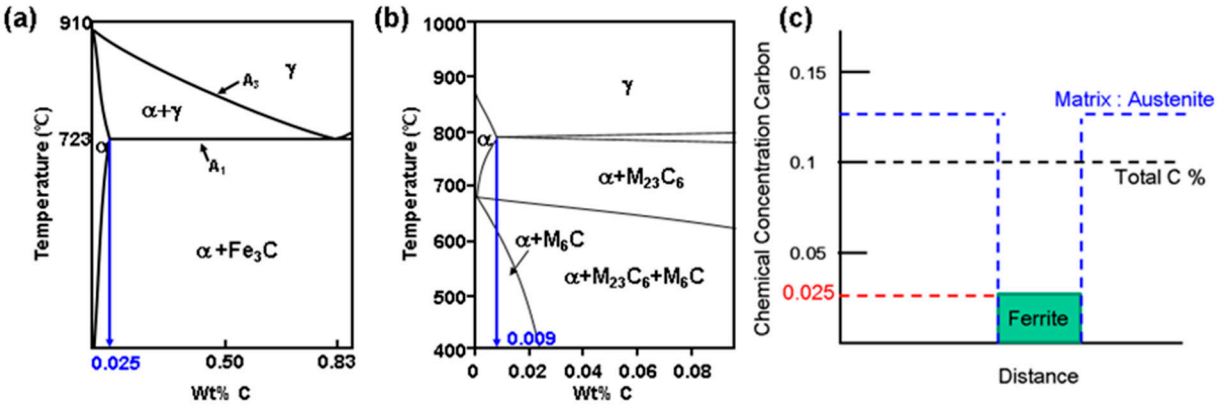

Fig.13 Schematic of calculation of carbon contents in matrix (a) Fe-C phase diagram (b) 2.25Cr-1Mo Steel + C phase diagram calculated using Thermo-calc (b) modeling of carbon concentration between ferrite and matrix

Fig. 14 shows the results of EPMA analysis of the 21 ft-lb impact specimen. It can be seen that there is a large amount of precipitate in the prior austenite grain boundaries. The precipitates consist of Cr, Mo, Mn and C, and in particular, precipitates with a higher content Cr and C were found. Usually, the precipitates with a higher content of Cr and C than M23C6 precipitates are supposed to be M7C3. In addition to forming incoherent boundaries between the matrix and precipitate by the HCP crystal structure, they form a surrounding Cr-depleted zone due to the high interrelation of Cr and C. Excess Cr-rich precipitates in the prior austenite grain boundaries cause Cr-depleted zone formation around the precipitate, which softens the grain boundaries and becomes vulnerable to corrosion as the Cr content decreases. It should also be noted that these precipitates may also affect the physical properties of the HAZ during welding.[111]

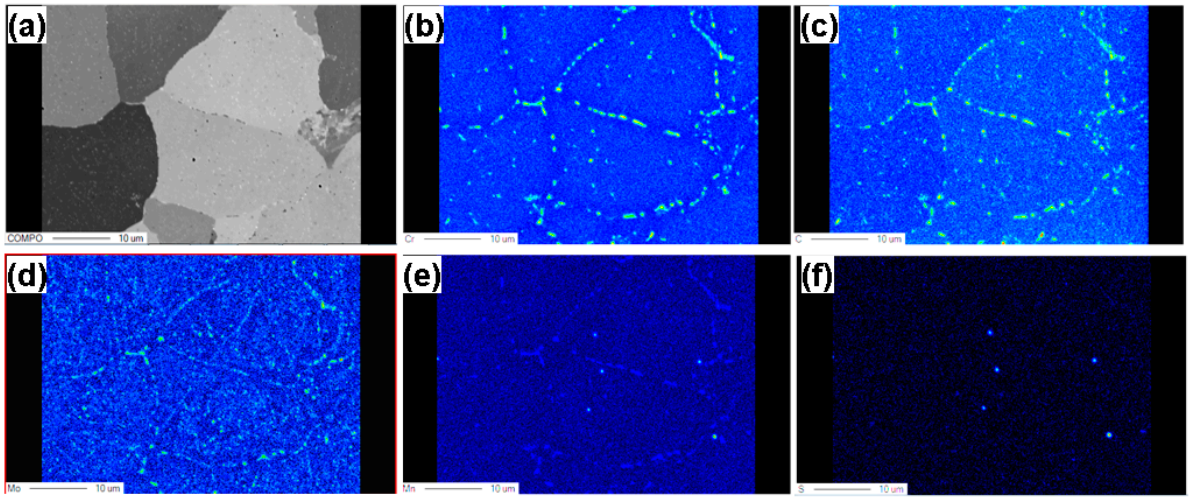

Fig.14 EPMA images of the 21 ft-lb impact specimen. (a) composite image (b) chromium (c) carbon (d) molybdenum (e) manganese (f) sulfur

4. Conclusions

The MnS and other inclusions in the 21ft-lb impact specimen were found to be larger than the 256ft-lb specimen. At the same cooling rate, the ferrite content of the base metal is increased as the ferrite deficient CCT curve moves to the left, due to the Mn deficiency caused by MnS formation. As the ferrite content increases, the impact value is lowered due to the decrease of the bainite, which has high impact test values. The increase of ferrite content increases the C content of other matrix, due to the low C content (0.025%) of ferrite (about 0.4798%), resulting in a large amount of precipitate (M23C6) in the PWN austenite grain boundaries, and coarse Cr precipitates are the migration path of cracks in micro-void generation. The occurrence of Cr-depleted zones leads to softening of the prior austenite grain boundaries, which can be expected to weaken the corrosion of these areas.

Acknowledgments: This work was supported by a National Research Foundation of Korea (NRF) grant funded by the Korea government (MSIP) (No. 2012R1A5A1048294).

Author Contributions: : Sanghoon Lee and Chungyun Kang conceived and designed the experiments. Hyesung Na performed the experiments and analyzed the data.

Conflicts of Interest: The authors declare no conflict of interest. The funding sponsors had no role in the design of the study; in the collection, analyses, or interpretation of data; in the writing of the manuscript, and in the decision to publish the results.

References

1. VISWANATHAN, R.; BAKKER, W. Materials for ultrasupercritical coal power plants—Boiler materials: Part 1. Journal of Materials Engineering and Performance, 2001, 10.1: 81-95.

2. MASUYAMA, Fujimitsu. History of power plants and progress in heat resistant steels. ISIJ international, 2001, 41.6: 612-625.

3. Viswanathan, R., Coleman, K., & Rao, U. Materials for ultra-supercritical coal-fired power plant boilers. International Journal of Pressure Vessels and Piping, 2006, 83.11-12: 778-783.

4. Ray, A.K., Tiwari, Y. N., Roy, P. K., Chaudhuri, S., Bose, S. C., Ghosh, R. N., & Whittenberger, J. D. Creep rupture analysis and remaining life assessment of 2.25 Cr–1Mo steel tubes from a thermal power plant. Materials Science and Engineering: A, 2007, 454: 679-684.

5. KLUEH, R. L.; NELSON, A. T. Ferritic/martensitic steels for next-generation reactors. Journal of Nuclear Materials, 2007, 371.1-3: 37-52.

6. DHOOGE, A.; VINCKIER, A. Reheat cracking—a review of recent studies. International Journal of Pressure Vessels and Piping, 1987, 27.4: 239-269.

7. DHOOGE, Alfred; VEKEMAN, J. New generation 2 1/4 Cr steels T/P 23 and T/P 24 weldability and high temperature properties. Welding in the World, 2005, 49.9-10: 75-93.

8. ARIVAZHAGAN, B.; VASUDEVAN, M. Studies on A-TIG welding of 2.25 Cr-1Mo (P22) steel. Journal of Manufacturing Processes, 2015, 18: 55-59.

9. BOILER, A. S. M. E.; CODE, Pressure Vessel. Section VIII Division 1. UG-126 Pressure Relief Valves to UG-129 Marking, ASME International, New York, 2010.

10. TOSHIRO, Kobayashi; ISAMU, Yamamoto; MITSUO, Niinomi. Evaluation of dynamic fracture toughness parameters by instrumented Charpy impact test. Engineering Fracture Mechanics, 1986, 24.5: 773-782.

11. YANG, Zhaorui; KANG, Hansaem; LEE, Youngseog. Experimental study on variations in charpy impact energies of low carbon steel, depending on welding and specimen cutting method. Journal of Mechanical Science and Technology, 2016, 30.5: 2019-2028.

12. LUCON, Enrico; MCCOWAN, Chris N.; SANTOYO, Raymond L. Instrumented impact tests: effects of machine variables and specimen position. Journal of Testing and Evaluation, 2008, 37.1: 59-68.

13. KURISHITA, Hiroaki, et al. Effects of V-notch dimensions on Charpy impact test results for differently sized miniature specimens of ferritic steel. Materials Transactions, JIM, 1993, 34.11: 1042-1052.

14. Im, Y. R., Oh, Y. J., Lee, B. J., Hong, J. H., & Lee, H. C. Effects of carbide precipitation on the strength and Charpy impact properties of low carbon Mn–Ni–Mo bainitic steels. Journal of nuclear materials, 2001, 297.2: 138-148

15. Sun, C., Fu, P. X., Liu, H. W., Liu, H. H., & Du, N. Y. Effect of Tempering Temperature on the Low Temperature Impact Toughness of 42CrMo4-V Steel. Metals, 2018, 8.4: 232. KLUEH, R. L.; ALEXANDER, D. J. Effect of heat treatment and irradiation temperature on impact properties of Cr–W–V ferritic steels1. Journal of Nuclear Materials, 1999, 265.3: 262-272.

16. Shen, D. D., Song, S. H., Yuan, Z. X., & Weng, L. Q. Effect of solute grain boundary segregation and hardness on the ductile-to-brittle transition for a Cr–Mo low-alloy steel. Materials Science and Engineering: A, 2005, 394.1-2: 53-59.

17. Hwang, B., Kim, Y. G., Lee, S., Kim, Y. M., Kim, N. J., & Yoo, J. Y. Effective grain size and Charpy impact properties of high-toughness X70 pipeline steels. Metallurgical and materials transactions A, 2005, 36.8: 2107-2114.

18. GHOSH, A., et al. Effect of microstructural parameters, microtexture and matrix strain on the Charpy impact properties of low carbon HSLA steel containing MnS inclusions. Materials Science and Engineering: A, 2014, 613: 37-47.

19. MELCHERS, Robert E.; CHAVES, Igor A.; JEFFREY, Robert. A Conceptual Model for the Interaction between Carbon Content and Manganese Sulphide Inclusions in the Short-Term Seawater Corrosion of Low Carbon Steel. Metals, 2016, 6.6: 132.

20. SPEICH, G. R.; SPITZIG, W. A. Effect of volume fraction and shape of sulfide inclusions on through-thickness ductility and impact energy of high-strength 4340 plate steels. Metallurgical Transactions A, 1982, 13.12: 2239-2258.

21. TSUNEKAGE, N.; TSUBAKINO, H. Effects of sulfur content and sulfide-forming elements addition on impact properties of ferrite–pearlitic microalloyed steels. ISIJ international, 2001, 41.5: 498-505.

22. CHERUVU, N. S. Degradation of mechanical properties of Cr-Mo-V and 2.25 Cr-1Mo steel components after long-term service at elevated temperatures. Metallurgical Transactions A, 1989, 20.1: 87-97.

23. LAHA, K.; RAO, K. Bhanu Sankara; MANNAN, S. L. Creep behaviour of post-weld heat-treated 2.25 Cr-1Mo ferritic steel base, weld metal and weldments. Materials Science and Engineering: A, 1990, 129.2: 183-195.

24. Mitra, R., Srivastava, A. K., Prasad, N. E., & Kumari, S. Microstructure and mechanical behaviour of reaction hot pressed multiphase Mo–Si–B and Mo–Si–B–Al intermetallic alloys. Intermetallics, 2006, 14.12: 1461-1471.

25. GARRISON JR, Warren M.; WOJCIESZYNSKI, Andrzej L. A discussion of the effect of inclusion volume fraction on the toughness of steel. Materials Science and Engineering: A, 2007, 464.1-2: 321-329.

26. MURAKAMI, Yukitaka. Material defects as the basis of fatigue design. International Journal of Fatigue, 2012, 41: 2-10.

27. Yokomizo, T., Enomoto, M., Umezawa, O., Spanos, G., & Rosenberg, R. O.. Three-dimensional distribution, morphology, and nucleation site of intragranular ferrite formed in association with inclusions. Materials Science and Engineering: A, 2003, 344.1-2: 261-267.

28. Zhang, C., Xia, Z. X., Yang, Z. G., & Liu, Z. H.. Influence of prior austenite deformation and non-metallic inclusions on ferrite formation in low-carbon steels. Journal of Iron and Steel Research, International, 2010, 17.6: 36-42.